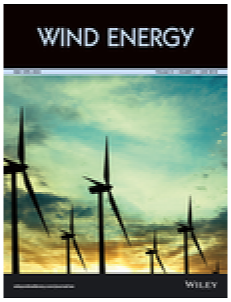

Offshore wind farm wake recovery: Airborne measurements and its representation in engineering models

Journal:	*Wind Energy*
Manuscript ID	Draft
Wiley - Manuscript type:	Research Article
Date Submitted by the Author:	n/a
Complete List of Authors:	Cañadillas, Beatriz; UL International Germany GmbH, R&D Foreman, Richard; UL International GmbH Barth, Volker; UL International Germany GmbH Siedersleben, Simon; Karlsruher Institut fur Technologie Institut fur Meteorologie und Klimaforschung Lampert, Astrid; TU Braunschweig Platis, Andreas; Eberhard-Karls-Universität Tübingen, Djath, Bughsin; Helmholtz-Zentrum Geesthacht Zentrum fur Materialforschung und Kustenforschung Schulz-Stellenfleth, Johannes; Helmholtz-Zentrum Geesthacht Zentrum fur Materialforschung und Kustenforschung Bange, Jens; Eberhard-Karls-Universität Tübingen Emeis, Stefan; Karlsruhe Institute of Technology, Institute of Meteorology and Climate Research Neumann, Thomas; UL International GmbH
Keywords:	offshore wind farm cluster, wake recovery, atmospheric stability, wind farm efficiency

Received: Added at production | Revised: Added at production | Accepted: Added at production

DOI: xxx/xxxx

ARTICLE TYPE

Offshore wind farm wake recovery: Airborne measurements and its representation in engineering models

Beatriz Cañadillas | Richard Foreman | Volker Barth | Simon K Siedersleben | Astrid Lampert | Andreas Platis | Bughsin Djath | Johannes Schulz-Stellenfleth | Jens Bange | Stefan Emeis | Thomas Neumann

[1]Renewable,UL International GmbH, Oldenburg, Germany
[2]Institute of Meteorology and Climate Research, Atmospheric Environmental Research (IMK-IFU), Karlsruhe Institute of Technology, Garmisch-Partenkirchen, Germany
[3]Institute of Flight Guidance, Technische Universität Braunschweig, Braunschweig, Germany
Environmental Physics (ZAG), University of Tübingen, Tübingen, Germany
Institute for Coastal Research, Helmholtz Zentrum Geesthacht, Geesthacht, Germany

Correspondence
*Beatriz Cañadillas, PhD, Email: beatriz.canadillas@ul.com

Present Address
Kasinoplatz 3, 26122 Oldenburg, Germany.

Summary

We present an analysis of wind measurements from a series of airborne campaigns conducted to sample the wakes from two North Sea wind farm clusters, with the aim of determining the dependence of the downstream wind speed recovery on the atmospheric stability. The consequences of the stability dependence of wake length on the expected annual energy yield of wind farms in the North Sea are assessed by an engineering wake model. The wakes are found to persist for significantly longer downstream distances ($>$ 50 km) in stable conditions than in neutral and unstable conditions ($<$ 15 km). The parameters of one common engineering model were modified to reproduce the observed wake decay at distances $>$ 30km. Larger reductions are expected for wind farms separated by $<$ 30km, which is generally the case in the North Sea, but additional data would be required to validate the required parameter modifications within the engineering model. Based on this, a case study is performed to show reductions in the farm efficiency downstream of a wind farm. These results emphasize not only the importance of understanding the stability climatology of offshore wind farms but also the need to update the representation of wakes in current industry models to properly include wake-induced energy losses, especially in large offshore clusters.

KEYWORDS:
offshore wind farm cluster, wake recovery, atmospheric stability, wind farm efficiency

1 | INTRODUCTION

As offshore wind farms in the North Sea are generally arranged in clusters because of spatial limitations and as a means of sharing infrastructure [1,2], wind farm wakes may be impinging on neighbouring areas, and reducing the expected energy yields of nearby installations. The wind speed recovery (also referred to as the wake recovery) within or directly behind very large wind farms has been the focus of analytical, experimental [3,4,5,6,2] as well as numerical investigations [7], while the lengths of wind farm wakes, as opposed to wakes from individual wind turbines, were originally observed with the help of satellite imagery [8], and others have continued this line of investigation [9,10]. More recently, Platis et al. [11] conducted an airborne campaign to make direct observations of these wakes, with the aim of assessing the dependence of wake length on boundary-layer parameters, such as the atmospheric stability. In coastal environments, such as the North Sea, airflow from the land on warm days brings warmer air over the cooler sea surface, resulting in large air–sea temperature gradients of up to 10°C [12,13]. Such a situation leads to stable conditions consisting of low turbulence as any roughness-generated vertical turbulent motion is damped by the stratified flow. For this reason, the wakes from wind farms in stable conditions are expected to persist further downstream as the vertical exchange of momentum between the wake layer and the undisturbed flow above is impeded by the stratified flow towards the surface[6].

In the wind energy industry, where engineering model suites are widely used due to their low computational costs and ease of use, direct wake effects are still mostly modelled by simplified models ("bottom-up models") of the Jensen/Park type[14,15], or the slightly more complex model of Ainslie[16]. Some suites also provide a model for the formation of an internal boundary layer (IBL) triggered by large offshore wind farms, which lowers the observed wind speeds inside the farm significantly below the levels calculated from the direct wake models alone[17,18]. These boundary-layer models treat the wind farm as an area of increased roughness depending on the actual wind farm geometry. The calculated energy yield inside an offshore wind farm thus depends on the interplay and the parametrization of both the direct wake model and the internal boundary-layer model[19,20]. Importantly, as the direct wake models and as well as the internal boundary-layer models we are aware of have been developed assuming neutral conditions and are independent of atmospheric stability, any changes induced by stability effects need to be explicitly accounted for by adjusting some parameters in the wake models to match the observations[21]. Since stable condition occur approximately 37% of the time in the North Sea[1], understanding the effect of stability on wake recovery is crucial for the accurate estimation of energy production. In this context, the WIPAFF project[1] was initiated to collect data of the wind speed within the wakes generated by wind farm clusters in the North Sea using a research aircraft operated by the Technische Universität Braunschweig in combination with in situ measurements, surface lidar measurements and satellite observations.

While several methodologies have been explored to measure the wind speed reduction and spatial extent of wakes, they have their limitations. For example, meteorological masts[22,23,24,25], dual-Doppler radar technology[2], and scanning Doppler lidar[26] provide high-resolution data, but are limited by their fixed locations so that they can only measure wakes for certain wind directions and at limited distances from the wind farm. Satellite-based synthetic aperture radar (SAR) observations[27,28,9,10] enable the measurement of wakes over larger areas, but the spatial resolution of the raw images limits the level of detail that can be observed. Direct aircraft observations[11] combine the advantages of in situ measurements directly within the wake with a large spatial coverage.

So far, the WIPAFF data have been compared with the wakes inferred from satellite measurements[9], and those simulated with mesoscale numerical weather prediction models[29,30]. However, the results of the airborne campaign have not yet been analysed and summarized in a form suitable for direct implementation in engineering models, with the view of assessing the expected reduced energy yields of downstream wind farms. Therefore, we present an analysis of the airborne measurement campaign summarised in[11], with the focus here on determining the dependence of the wind speed recovery in wakes on stability for application in the modelling of wind farm energy production by the engineering models. Based on our these results, we adjust the wind speed recovery function in the WindFarmer model[18] and analyze the effects on wind farm efficiency.

Below, Section 2 briefly considers the theoretical formulation of wake recovery, which provides a useful basis for understanding the key parameters governing the wake length, including their dependency on atmospheric stability. Section 3 provides a description of the airborne measurement campaign. Section 4 describes the analysis of the wake measurements obtained from the flights in the North Sea, and the results of the analysis are presented in Section 5. Based on these results, Section 6 addresses the representation of the wind speed recovery in the Windfarmer model[18], with a view to estimating the impacts of offshore wakes on the energy production on downstream wind farms. The conclusions of our investigation are presented in Section 7.

2 | THEORETICAL CONSIDERATIONS

Analytical models exist for the estimation of the wake length from wind farms of infinite horizontal extent[3,4,5,6,21]. To give an impression of the important parameters governing the lengths of wakes behind very large wind farms as a function of the distance downstream x, Figure 1 shows the wind speed recovery $U_R = U/U_\infty$ according to Equation 5 in Appendix A, where U is the wind speed within the wake and U_∞ is the freestream wind speed.

The following parameters have been assumed for offshore conditions: the roughness length $z_0 = 1 \times 10^{-4}$ m, freestream wind speed $U_\infty = 10\,\mathrm{m\,s^{-1}}$, friction velocity $u_* = 0.3\,\mathrm{m\,s^{-1}}$[31], ambient turbulence intensity $I_u = 8\%$ (corresponding to the 5-year average of the undisturbed flow in the North Sea at the FINO1 research platform at 100 m above the surface), hub height $h = 90$ m, wind-turbine thrust coefficient $C_T = 0.8$, and turbine diameter $D = 120$ m. The multiple curves correspond to the Monin–Obukhov stability parameters $z/L = [-1, 0, 0.25, 1]$ (see Appendix B) for unstable, neutral, stable, and very stable conditions, respectively, for the wind-turbine spacings $s/D = 6$ (a) and $s/D = 10$ (b). Figure 1(c) shows the wind speed recovery for constant $z/L = 0.25$, but for different rotor diameters $D = 100$ m and $D = 200$ m and the spacings $s/D = 6$ and 10.

Assuming the wake length corresponds to a value of wind speed recovery $U_R = 0.95$, Figure 1(a) shows wake lengths in unstable, neutral, and stable conditions ($z/L = -1, 0, 0.25$) of 10 km, 20 km, and $>$ 50 km, respectively. Increasing the turbine spacing within the wind farm increases the initial wind speed in the wake U_0, which reduces the wake length for all stabilities (Figure 1b). For example, the initial wind speed recovery $U_R(x = 0) = 0.32$ for $z/L = 1$ and a spacing $s/D = 6$ (Figure 1a) reduces to $U_R(x = 0) = 0.58$ for $z/L = 1$ for an increased spacing of $s/D = 10$

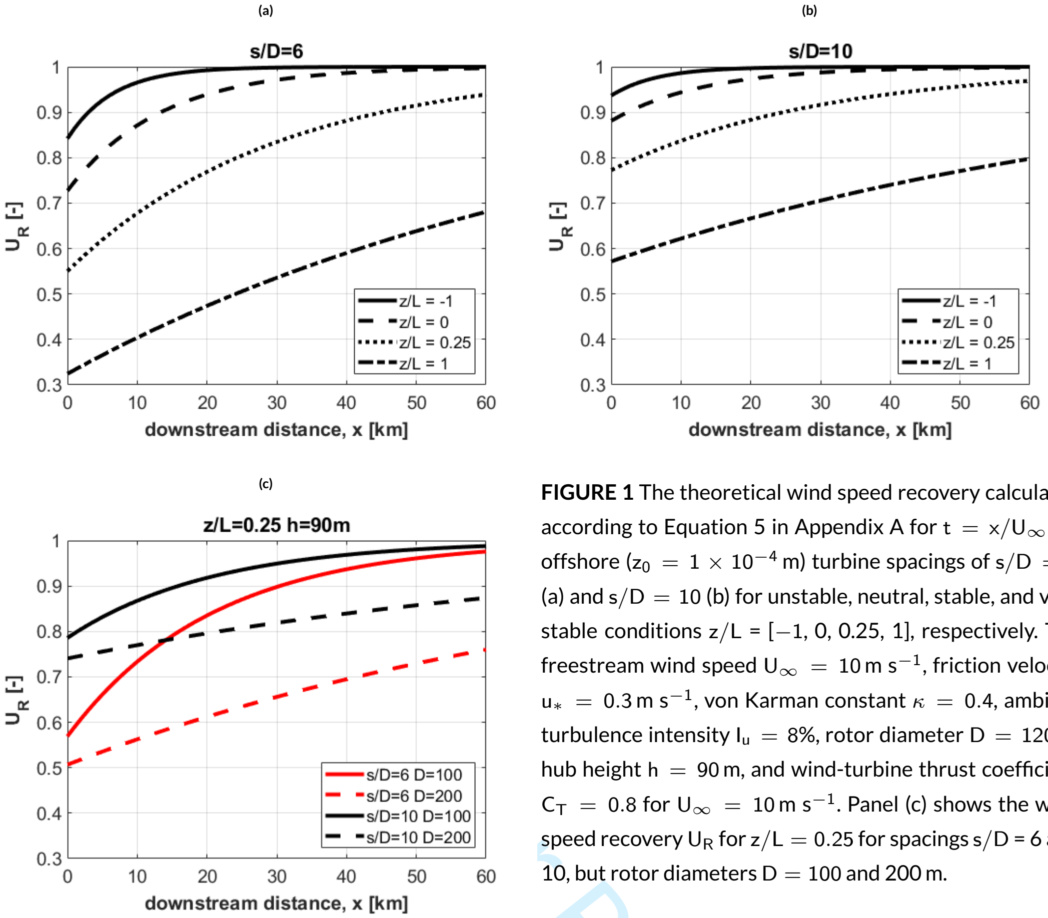

FIGURE 1 The theoretical wind speed recovery calculated according to Equation 5 in Appendix A for $t = x/U_\infty$ for offshore ($z_0 = 1 \times 10^{-4}$ m) turbine spacings of $s/D = 6$ (a) and $s/D = 10$ (b) for unstable, neutral, stable, and very stable conditions z/L = $[-1, 0, 0.25, 1]$, respectively. The freestream wind speed $U_\infty = 10\,\mathrm{m\,s^{-1}}$, friction velocity $u_* = 0.3\,\mathrm{m\,s^{-1}}$, von Karman constant $\kappa = 0.4$, ambient turbulence intensity $I_u = 8\%$, rotor diameter $D = 120$ m, hub height $h = 90$ m, and wind-turbine thrust coefficient $C_T = 0.8$ for $U_\infty = 10\,\mathrm{m\,s^{-1}}$. Panel (c) shows the wind speed recovery U_R for $z/L = 0.25$ for spacings s/D = 6 and 10, but rotor diameters $D = 100$ and 200 m.

(Figure 1b), which is an equivalent value of $U_R\ (x = 0)$ for the reduced stability $z/L = 0.25$ with the spacing $s/D = 6$. The wind speed recovery rate β [$\mathrm{s^{-1}}$] (see Equation 10, Appendix A) decreases with increasing stability through the dimensionless wind shear ϕ_m, resulting in a reduced rate of wind speed recovery. Physically, this implies that the stability acts as a resistance to the entrainment of the freestream flow into the wake from above. In contrast, the value of β and the wind speed recovery U_R decreases with the inverse time scale $u_* h/D^2$ [$\mathrm{s^{-1}}$]. For example, as the rotor diameter D increases, the mixing scale over which vertical momentum exchange occurs according to Equation 2 in Appendix A must increase, which implies longer wakes in Figure 1(c) for a rotor diameter $D = 200$ m compared with $D = 100$ m.

3 | DESCRIPTION OF THE AIRBORNE MEASUREMENT CAMPAIGN

From September 2016 until October 2017, a series of airborne measurement campaigns (see Platis et al.[11] for a campaign summary) were conducted by the Technische Universität Braunschweig using the research aircraft Dornier DO 128-6[32]. The DO 128 research aircraft records micro-meteorological data at 100 Hz using a nose boom equipped with sensors for the detection of, among other parameters, the flow velocity with a multi-hole flow probe with an inertial motion correction, and temperature, barometric pressure, and relative humidity. Aircraft descent to ∼50 m and ascent to ∼1000 m above the sea surface enables sampling of the boundary-layer properties of the flow surrounding the wind farm. The aim of the campaign was to quantify wind farm cluster wakes in the North Sea for stable and unstable conditions[1]. While the measured data enable investigation of a broad range of meteorological phenomena[30], our focus here is on the wind speed recovery of wakes downstream of wind farm clusters, and the dependence on stability.

The left inset of Figure 2 presents an example of a flight path downstream of the N-4 wind farm cluster performed on 10 September 2016, which includes the Amrumbank West, Nordsee Ost and Meerwind Süd/Ost wind farms (see Table 1 for a summary of the key characteristics of the wind farms within the N-3 and N-4 clusters investigated here). Note that all wind farms (marked as blue points in Figure 2) were in operation during all flight campaigns except the NordseeOne wind farm (to the west of Gode Wind 2), which started operation in September 2017. In the flight path

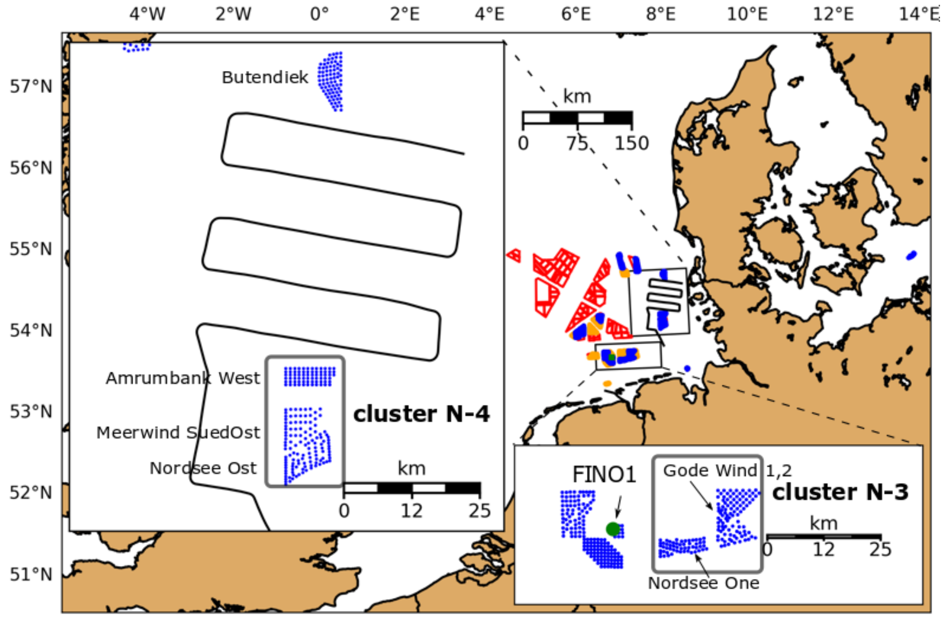

FIGURE 2 Existing (blue), planned (yellow) and future (red) wind farms in the German exclusive economic zone (EEZ) of the North Sea. The inset on the left side of the panel shows an example of a flight path carried out on 10 September 2016 at hub height downstream of the N-4 cluster (gray rectangle) and upstream of the Butendiek wind farm for wind flow from the south. The inset at the bottom of the panel gives a detailed view of the N-3 cluster (gray rectangle). The position of the 100-m high meteorological mast FINO1 is also indicated (green point). Wind farm coordinates have been obtained from[33].

TABLE 1 Properties of the wind farms within the N-3 and N-4 (cluster names are defined according the offshore areas specified by the German Federal Hydrographic Agency[34]), the turbine type within the wind farms, their rotor diameter D, hub height h, the number of wind turbines (N° WTG) and the range of spacings between wind turbines s/D.

Cluster ID	**Wind farm**	**Turbine Type**	D **[m]**	h **[m]**	**N° WTG**	s/D **[-]**
N-3	Gode Wind 1, 2	Siemens SWT-6MW	154	110	55, 42	6–12
N-3	Nordsee One	Senvion 6.2MW	126	90	54	5–9
N-4	Amrumbank West	Siemens SWT-3.6MW	120	90	80	5–6.5
N-4	Nordsee Ost	Senvion 6.2MW	126	95–97	48	5–10
N-4	Meerwind SuedOst	Siemens SWT-3.6MW	120	90	80	4–12

shown in Figure 2, the wake length extended to the Butendiek wind farm, some >50 km north of the N-4 cluster. The wake traversals at progressive distances behind the cluster sampled the wake recovery downstream of the N-4 cluster by traversing the wake five times perpendicular to the main wind direction. Additional vertical profiling up to altitudes of 1000 m upstream, downstream and lateral to the wake probed the boundary-layer properties.

Out of 42 flights (see Platis et al.[11]), the 11 selected for analysis have approximately steady freestream flow conditions at average offshore wind speeds ($U_\infty \approx 10\,\mathrm{m\,s^{-1}}$), flight altitudes at approximately hub height ($h \approx 100$ m), and a minimum of four wake traversals at various downstream distances. Table 2 summarizes a number of key parameters characterizing each flight.

Included in Table 2 is the Monin–Obukhov stability parameter z/L estimated from the bulk Richardson number R_{bv} which calculated according to Equation 21, see Appendix B) based on the freestream wind speed U_∞ and the virtual potential temperature difference $\overline{\theta}_v - T_{v0}$. Here, $\overline{\theta}_v$ is the virtual potential temperature at flight altitude and T_{v0} is the virtual temperature at the sea surface (see Appendix B). The turbulent kinetic energy (TKE) in Table 2 corresponds to free wind stream at hub height see[11].

TABLE 2 Summary of the 11 airborne experimental campaigns in the North Sea considered here, showing the flight duration (corresponding to the wake-traversal period), freestream wind speed U_∞, wind direction (WDir), virtual potential temperature $\overline{\theta}_v$, surface virtual temperature T_{v0}, Monin–Obukhov stability parameter z/L, turbulent kinetic energy (TKE), power-law exponent α; vertical profiles not low enough on 7 September 2016 (N/A) to obtain realistic values of α). The cluster ID corresponds to the particular cluster specified in Table 1.

ID	**Date** (d-mmm-yy)	**Flight Period** [UTC]	U_∞ [$\mathrm{m\,s^{-1}}$]	**WDir** [°]	$\overline{\theta}_v$ [°C]	T_{v0} [°C]	z/L [-]	**TKE** [$\mathrm{m^2\,s^{-2}}$]	$1/\alpha$ [-]	**Cluster ID**
1	6-Sep-16	12:40–14:40	8	190	19.5	19.2	0.2	0.2	4	N-4
2	7-Sep-16	12:25–13:05	4	190	20.3	19.2	2.5	0.1	N/A	N-4
3	10-Sep-16	08:10–09:30	8	190	19.7	18.8	0.5	0.2	3	N-4
4	5-Apr-17	15:00–16:25	13	310	8.2	8.8	−0.1	0.9	4	N-3
5	11-Apr-17	14:35–15:40	9	260	8.2	8	0.1	0.2	8	N-3
6	27-May-1 7	09:00–11:00	10	150	18.7	15.9	1.1	0.1	2	N-4
7	27-May-17	15:05–16:10	12	140	23.5	21.3	0.5	0.1	2	N-4
8	8-Aug-17	13:30–15:20	15	80	22	20.1	0.3	0.5	3	N-4
9	14-Aug-17	15:00–17:20	8	120	18.2	18.5	−0.1	0.4	12	N-4
10	15-Aug-17	08:15–09:15	7	180	19.9	18.9	1.0	0.1	9	N-3
11	15-Oct-17	12:30–14:15	12	190	18.2	16.5	0.6	0.2	4	N-3

The power-law exponent α is calculated from the power-law wind speed profile

$$\frac{U_z}{U_{ref}} = \left(\frac{z}{z_{ref}}\right)^{\alpha}, \tag{1}$$

where the U_{ref} is the reference wind speed at $z_{ref} = 100$ m. An average value of α is calculated from the aircraft-derived wind speed profiles upstream and downstream of the cluster wake for altitudes encompassing the rotor plane.

4 | WAKE-DETECTION METHODOLOGY

The horizontal extent of the cluster wake may be reconstructed by inspection of the wind speed profiles at approximately hub height at varying distances downstream of the cluster. An example of the wake-traversal strategy is shown in Figure 3, illustrating the flight path around and downstream of the N-4 cluster for a total of seven traversals of the cluster wake perpendicular to the mean wind direction (150°) on 27 May 2017.

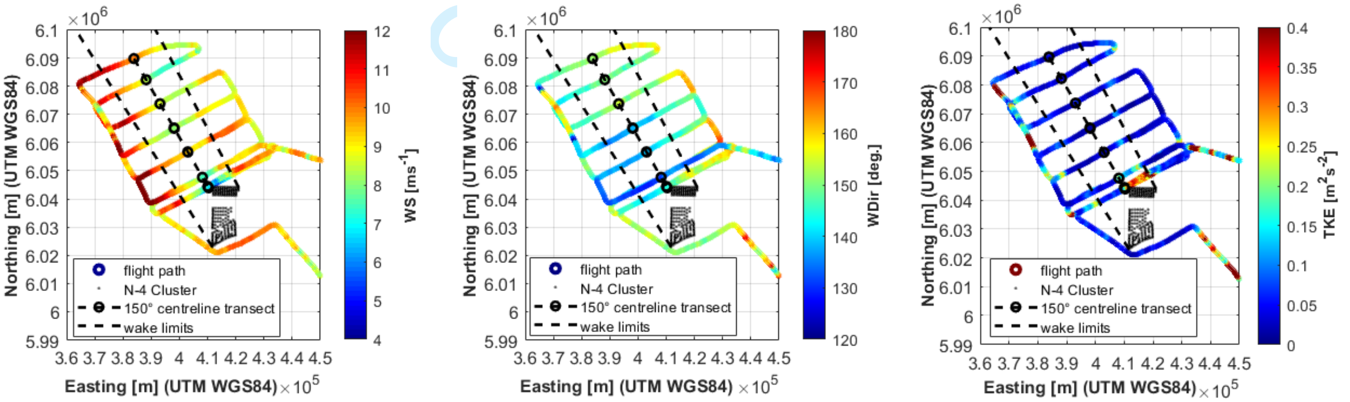

FIGURE 3 The flight path in the vicinity of the N-4 cluster (individual turbines as black points) from 09:00 to 11:00 UTC on 27 May 2017 (ID = 6) showing (from left to right) the wind speed (WS), wind direction (WDir) and TKE according to the colour scale shown to the right of each panel. The dashed lines denote the approximate wake limits, and the dotted/dashed line marked with black circles is aligned with the wind direction of 150°. The flight altitude in the traversals of the wake cluster is 95 m. The horizontal dimensions are indicated in UTM coordinates [m]. See Figure 2 for the position of this cluster with respect to the North Sea coast.

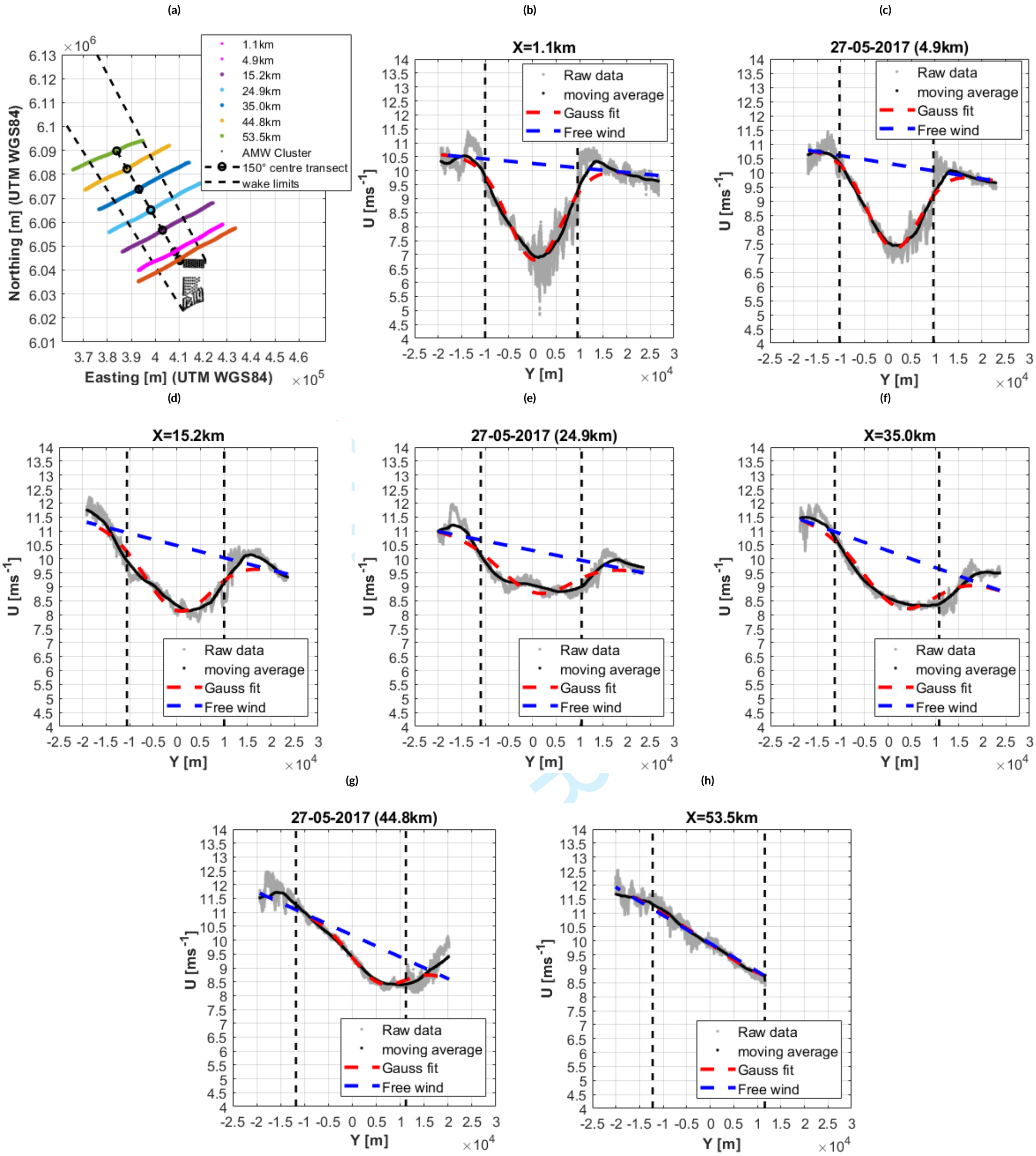

FIGURE 4 Horizontal wind speed profiles during strong stable conditions ($z/L \approx 1.1$) at several downstream distances x, while y denotes the position along the traversal. The flight took place approximately at hub height $z \approx 95$ m from 09:00–11:00 UTC on 27 May 2017. Panel a shows the wake traversals perpendicular to the nominal wind direction of 150° (black circles are the centreline positions) downstream of the N-4 cluster, and the approximate extent of the wake based on the edges of the cluster (dashed lines). The horizontal coordinates are given in UTM coordinates, the west–east extension of the cluster (black points) is 10 km. The wind speed measured during each traversal corresponds to the wind speed profiles in the corresponding panel (see the panel title for the respective downstream distance x). The gray curves in panels b through h represent the 100-Hz data, the black line shows the data filtered by a moving average, the red dashed curve is the Gaussian fit to the filtered curve as described in the main text, the blue dashed curve is the estimated wind speed gradient of the freestream wind speed $U_\infty = 10\,\mathrm{m\,s^{-1}}$, and the black dashed vertical lines represent the estimated wake width based on the horizontal cluster extent.

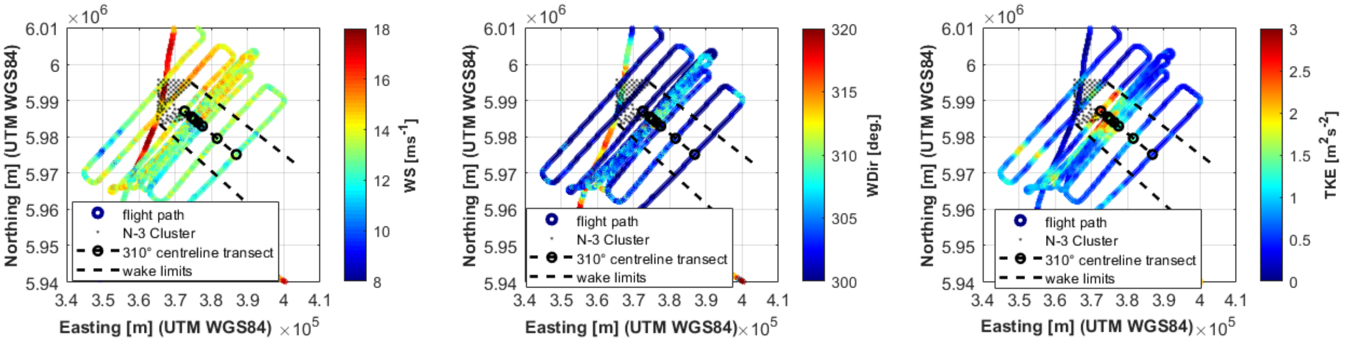

FIGURE 5 The flight path in the vicinity of the N-3 cluster (individual turbines as black points) from 13:30–16:30 UTC on 5 April 2017 showing (from left to right) the wind speed, wind direction and TKE according to the colour scale shown to the right of each panel. The dashed lines indicate the approximate wake limits, and the dotted line marked with black circles gives the wake centreline aligned with the wind direction of 310°. The flight altitude in the traversals of the wake cluster is 120 m.

Each panel indicates (from left to right) the wind speed, wind direction and TKE, as indicated by the colour bar to the right of each panel. The flight altitude is approximately 95 m, corresponding to the hub height of the 3.6 MW Siemens wind turbines (Table 1), and the wind direction is from the south-east, corresponding to a fetch of approximately 75 km to the coastline. Such flow conditions in May generally bring warmer air from the land over the colder North Sea water, leading to the highly stable conditions that are expected to produce long wakes, and a slow wind speed recovery. The dashed lines extending from the corners of the cluster in Figure 3 indicate the geometrically estimated horizontal wake extent, while the central dotted–dashed line is the estimated wake centreline, assuming a constant mean wind direction (150°) for the flight period. The wind farm layout is asymmetric with respect to the centreline of the cluster wake for this wind direction, implying a horizontally asymmetric wake structure.

The central panel of Figure 3 indicates that the wind direction deviates slightly from the nominal value of 150° in both space and time (for the traversals perpendicular to the wake). For example, the traversal upstream of the N-4 cluster shows a wind-direction variation of approximately 10° (the larger wind-direction and TKE variations shown in red are vertical boundary-layer profiling manoeuvres of the aircraft up to 1000 m in altitude). The wind speed is spatially inhomogeneous, even outside of the wake.

The measured 100-Hz horizontal wind speed during the flight path traversals of Figure 3 are shown in grey in Figure 4, where each of the panels (b)–(h) represents one of the traversals shown in Figure 4a. The downstream distance x of each profile is stated in the respective panel title. The approximate freestream wind speed is indicated as the blue dashed line, assuming a linear horizontal background wind gradient along each traversal based on the wind speed outside the wake limits (dashed lines). The solid black lines are the 100-Hz data filtered by a moving average with a window size corresponding to the width of the estimated wake half-width, whose purpose is to filter turbulent fluctuations that would otherwise bias the shape of the fitted wind speed profile to regions of higher turbulence.

Assuming a self-similar behaviour of the wind speed within the wake cross-section[35], a Gaussian function of the form

$$F(y) = \exp\left(\frac{-(y - y_{\min})^2}{2\sigma_y}\right), \tag{2}$$

is fitted (red dashed line in Figure 4) to the filtered wind speeds within the wake, where y is the coordinate in the direction of the flight path, $y_{\min}$ is the position of the wake minimum according to the Gaussian fit, and σ_y denotes the standard deviation of the mean wind speed deficit in the span-wise direction at each cross-section and is treated as the wake width. The parameters $y_{\min}$ and σ_y are determined from the function $F(y)$ that minimizes the squared difference of the filtered horizontal wind speed profile, with the resulting curves indicated as the red dashed lines in Figure 4.

A clear wake signal with a minimum wind speed $U_{\min}$ = 7 m s^{-1} is evident in the first traversal $x = 1.1$ km downstream of the N-4 cluster, while the freestream wind speed is estimated as $U_\infty = 10$ m s^{-1} at $y \approx 0$ (see Figure 4). Due to the asymmetric orientation of the N-4 cluster with respect to the traversals, the western side of the cluster is located further, upstream relative to the flight legs. Therefore, the wake recovery west of the wake center has already progressed further so that wind speeds west of the wake center are already higher than to the east (cf. Figure 4). In general, note that the value of U_∞ may vary over the course of each flight campaign. As discussed by Frandsen et al.[22], depending on the size of the cluster and the length of the wake, mesoscale flow variations are also possible in the time the flow needs to traverse the cluster; these variations may result from land–sea gradients[2]. Also note that the wind farms in the N-4 cluster have a wide range of separations $s = x/D$ as presented in

Table 1, and the orientation of the turbines relative to the wind direction is staggered. Throughout the wake recovery, a speed up appreciable at the ridges of the wind park cluster limits may be due to the change of surface roughness between the wake and the free stream flowarea.

An example of a flight pattern for unstable conditions is presented in Figure 5 for the N-3 cluster on 5 April 2017, when a nominal wind direction of 310° brought cooler air from the north over the relatively warmer North Sea water towards the coast, leading to unstable conditions. As a shorter wake length was expected for the flow on this day, the flight traversals of the wake are more densely spaced directly behind the N-3 cluster. The larger magnitude of the TKE is also evident in the measurements (see Figure 5, right panel), particularly in the wake, where TKE values up to $3\,\mathrm{m}^2\,\mathrm{s}^{-2}$ are detected in the near field. For these magnitudes of turbulence, wakes tend to dissipate more rapidly because of the more efficient mixing between the wake flow and the freestream flow. The wind direction is relatively constant, but a slight horizontal wind gradient is detected in the undisturbed flow for the flight traversals behind the wind farm cluster.

Figure 6 shows the horizontal wind speeds along the wake traversals of the N-3 cluster on 5 April 2017 during unstable conditions. Compared with the profiles of Figure 4 obtained during stable conditions on 27 May 2017, the magnitude of turbulence is greater in Figure 6. From the moving-averaged signal (black line) in Figure 6, there is a wake profile evident within the turbulence, which is fitted with Gaussian profiles as outlined above. The wake signal extracted from the turbulence appears to have almost completely recovered at $x = 16.7$ km, although there is also an asymmetric wake recovery for this case, since the left side of the cluster is positioned a few kilometres further upstream of the first flight leg (see Figure 6g).

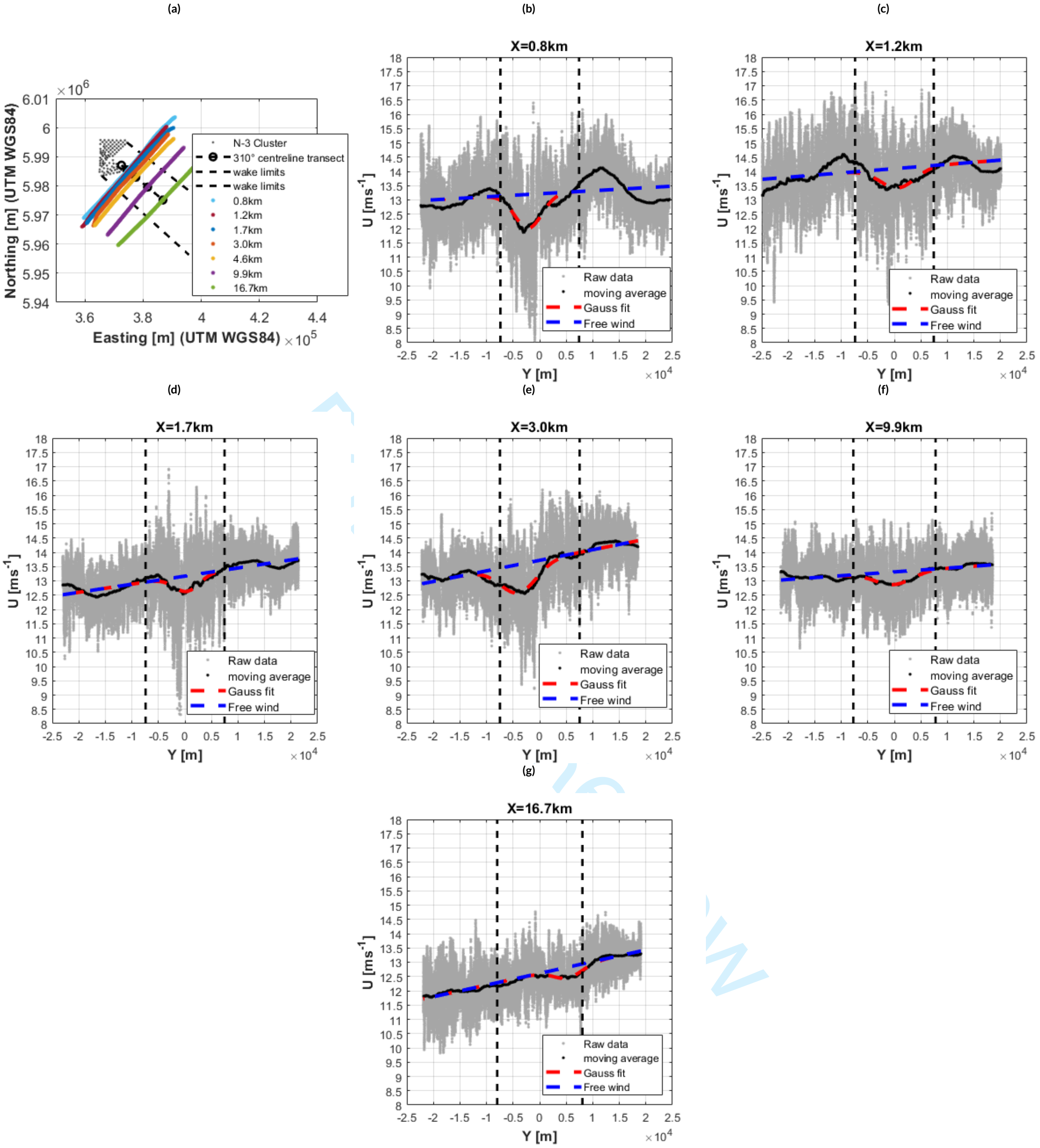

FIGURE 6 Horizontal wind speed profiles during unstable conditions ($z/L < 0.4$) at several downstream distances x, while y denotes the position along the traversal. The flight took place approximately at hub height $z \approx 120$ m from 14:35–15:40 UTC on 5 April 2017. Panel a shows the wake traversals perpendicular to the nominal wind direction of 310° (black circles are the centreline positions) downstream of the N-3 cluster, and the approximate extent of the wake based on the boundary of the cluster (dashed lines). The horizontal coordinates are given in UTM coordinates, the west–east extension of the cluster (black points) is 10 km. The wind speed measured during each traversal corresponds to the wind speed profiles in the corresponding panel (see the panel title for the respective downstream distance x). The grey curves in panels b through g represent the 100-Hz data, the black line shows the data filtered by a moving average, the red dashed curve is the Gaussian fit to the filtered curve as described in the main text, the blue dashed curve is the estimated wind speed gradient of the freestream wind speed $U_\infty = 13\,\mathrm{m\,s^{-1}}$, and the black dashed vertical lines represent the estimated wake width based on the horizontal cluster extent.

5 | WAKE-RECOVERY ANALYSIS

The two flights presented above give examples of the wind speed recovery in stable and unstable conditions, corresponding to relatively low and high values of turbulence as evident in the horizontal wind speed profiles in Figures 4 and 6, implying weak and strong turbulent exchange, resulting in relatively long and short wakes, respectively. To summarize the analysis of the wind speed recovery for the flights considered in Table 2, we define the wind speed recovery for the experimental data (cf. Equation 5 in Section 2) as

$$U_R(x) = \frac{U_{\min}(x)}{U_\infty(x, y_{\min})}, \tag{3}$$

where $U_{\min}(x)$ is the minimum value of the fitted Gaussian horizontal wind speed profile (for example, $U_{\min}(x = 44.8\,\mathrm{km}) \approx 8.4\,\mathrm{m\,s^{-1}}$ at the lateral position $y_{\min} \approx 0.75$ km Figure 4g). The freestream wind speed U_∞ is estimated for each horizontal wake traversal assuming a linear gradient between the wind speeds outside the estimated wake width. The value of U_∞ is taken at the lateral position of the minimum wind speed $y_{\min}$ (see the blue dashed lines in Figs. 4 and 6).

The wind speed recovery profiles $U_R(x)$ for both stable and unstable/neutral conditions as a function of the downstream distance x are found by assuming a nonlinear regression model of the form

$$U_R(x) = 1 - a\exp(-bx), \tag{4}$$

consistent with the expectation of Emeis[6] that the wind speed in the wake recovers exponentially as a function of the downstream distance x (see Equation 5). Here, a and b are empirical constants, where $a = 1 - U_R(x = 0)$ and $U_{R0} \equiv U_R(x = 0)$, while the flow recovery rate b corresponds to β as described by Equation 10 (after conversion to the space domain $t = x/U_\infty$). The empirical coefficients a and b are given in Table 3 for each of the 11 flights, and the black dashed lines in Figure 7 represent Equation 4 with the respective coefficients. The curves based on the median values of the coefficients a and b for the stable and neutral/unstable cases are shown in red in Figure 7, with the values of these coefficients also given in Table 3. To give some indication of the strength of the fits, the R^2 values and the values of the root-mean-square error are provided.

The stable cases with a median freestream wind speed $U_\infty \approx 10\,\mathrm{m\,s^{-1}}$ give an initial wind speed recovery compared to the freestream wind speed of

$$U_{R0} = \frac{U_{\min}(0)}{U_\infty} \approx 0.7. \tag{5}$$

The wake length is defined (based on the exponential fit) as the distance where the wind speed has recovered to 95% of the freestream wind speed ($U_R = 0.95U_\infty$, see Table 3 for the 95% wind speed recovery length for each case). The neutral case in Figure 7 (right) shows an initial wind speed recovery $U_{R0} = 0.8$ for a wake length of approximately 30 km, while the two unstable cases show almost complete recovery within the first 5km. These results support the hypotheses of Emeis[5,6] and Peña[21] that stable conditions lead to both a stronger wind speed deficit immediately downstream of the wind farm, and a slower wind speed recovery in the far field (see Figure 1). For the stable conditions, the median flow recovery rate $b = 0.033$, while for unstable/neutral conditions $b = 0.058$.

The furthest outliers from the median value of $b = 0.033$ in stable conditions include the two N-3 cluster cases 15 August 2017 (ID = 10, $b = 0.054$) and 15 October 2017 (ID = 11, $b = 0.012$), giving higher and lower values of b, respectively. The relatively higher wind speed recovery rate $b = 0.054$ for flight ID = 10 on 15 August 2017 has a value of b comparable to the unstable/neutral cases, but with an estimated Monin–Obukhov stability parameter at hub height $z/L \approx 1$ according to Table 2, which indicates clearly stable conditions, and is consistent with the initial wind speed recovery $U_{R0} = 0.74$ found for the other stable cases. However, the vertical wind shear during this campaign $1/\alpha = 9$ suggests near-neutral conditions ($1/\alpha = 11$ over water), and is thus inconsistent with stable conditions. Another point is that the position of the wake minimum $y_{\min}$ is displaced approximately 10 km to the west of the centreline placed along the 180° transect, which correlates with the turning of the wind speed from 170–230° from the beginning till the end of the wake traversals (not shown).

The relatively lower wind speed recovery rate $b = 0.012$ of the case on 15 October 2017 yields a very long wake length > 80 km. In contrast to the case on 15 August 2017, the wind direction was a relatively steady 190° during this flight, which, given also the stable conditions $z/L \approx 0.5$, made these atmospheric flow conditions ideal for the generation of a long wake. Although the stability is not unusually high in comparison with the other cases, this particular wake comes from the N-3 cluster, which, according to Table 1, contains wind turbines of larger rotor diameter D compared with the N-4 cluster. As seen in Figure 1, a larger rotor diameter at a given stability and hub height reduces the the wake decay rate β according to Equation 10 in Appendix A. Physically, this implies that the turbulent exchange between the wake at hub height and the freestream layer above occurs over a larger scale assuming $\Delta z \approx D$ in the formula for the wind speed recovery Equation 5, which reduces the efficiency of the wind speed recovery. *Further experiments are required to validate this hypothesis.* The wind speed recovery curves shown in red in Figure 7 are the summarized experimental results represented in the engineering model in Section 6 below. The wind speed recovers to 95% at a downstream distance of approximately 55 km for stable conditions (Figure 7, left), whereas the wind speed recovery to 95% of the freestream wind speed in neutral and unstable conditions extends to a distance of 20 km.

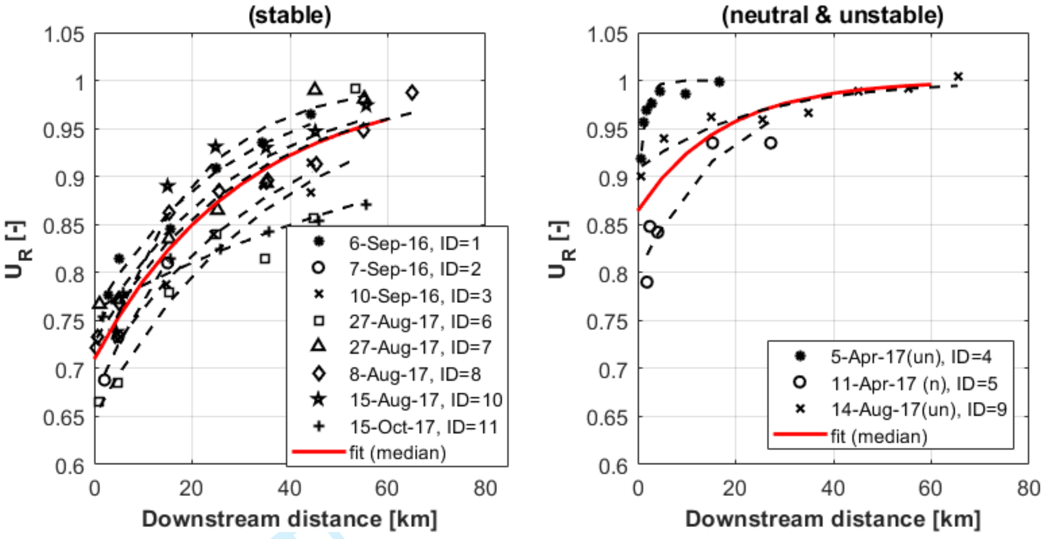

FIGURE 7 Wind speed recovery as a function of the downstream distance x [km]. Each data point indicates the wind speed recovery U_R at the minimum wake wind speed $U_{\min}$ for each flight leg at hub height (h $\approx$ 100 m) for stable (left) and unstable/neutral (right) stratification, based on the bulk Richardson number presented in Table 2. The dates in the panel captions also correspond with the dates listed in Table 2. The dashed curves are exponential fits to each case based on Equation 4. The red curves correspond to the exponential function applied to the median of all cases. See Table 3 for the values of the parameters a and b.

6 | REPRESENTATION OF WAKE-RECOVERY IN AN ENGINEERING MODEL

Here, we wish to address the question of how to represent the results of Figure 7 in engineering models for the purposes of determining the economic consequences of the wakes from wind farm clusters on downstream installations. The widely-used engineering software suite “WindFarmer (WF)”[18] is used as an example, which gives the option of the Jensen/PARK[14,15] or[16] wake models for individual wind turbines, and provides an IBL model for large wind farms, which considers them as a source of added surface roughness. At a specified position downstream x_{start} of the wind farm, the wind speed recovery is modelled explicitly as the power function

$$U_R = 1 - \left(1 - \frac{U}{U_\infty}\right) 0.5^{\left(\frac{x - x_{\text{start}}}{x_{50\%}}\right)}, \tag{6}$$

where x_{start} is the downstream distance specifying the start of the power function, and $x_{50\%}$ is the location where the wind speed recovery U_R has recovered to half its initial value. This function, which has been explicitly introduced by the WindFarmer developers as a heuristic guess without reference to an explicit physical process[18], enables adaption of the parameters to the airborne observations to wake regions within the model.

The direct wake models exhibit a relatively fast wind speed recovery. For example, application of the Jensen/PARK model[14,15] within the wind farm, with a wake decay constant $k = 0.04$ (a commonly used offshore value) predicts a wind speed deficit of $< 0.5\%$ at a distance of 15 km downstream, assuming a turbine rotor diameter of $D = 120$ m and thrust coefficient $c_t \leq 0.8$. Therefore, direct wake models hardly play a role when considering wakes at distances $x > 15$ km downstream of the wake-generating farm, as found for stable conditions.

The default set-up of the wake-recovery function in WindFarmer has been established based on observations from meteorological towers installed about 2 km and 6 km east of the offshore wind farms Horns Rev and Nysted, respectively[36]. As shown in Figure 8, these data match well with the results for the modelled wind speed recovery downstream of the N-4 cluster when using the “modified PARK” (Jensen) wake model for direct wakes, as well as the default settings of the internal boundary-layer model suggested by WindFarmer ($x_{\text{start}} = 60D$ and $x_{50\%} = 40D$; see the dashed lines in Figure 8; here, the rotor diameter $D = 120$ m). The agreement of the WindFarmer default settings with our fit to the airborne observations (red line in Figure 8 right) under neutral/unstable conditions is reasonable within the error range of our best fit, even though the default WindFarmer set-up seems to recover slightly too quickly. Since the WindFarmer default settings are designed for neutral conditions, they clearly underestimate the observed magnitude and extension of the wind speed deficit for wakes in stable conditions (see Figure 8 left). Our best approximation to the observed recovery is modelled by $x_{\text{start}} = 20D$ and $x_{50\%} = 100D$ for the neutral/unstable case (solid black line in Figure 8 right), and $x_{\text{start}} = 200D$ and $x_{50\%} = 200D$ for the stable case (solid black line in Figure 8 left).

TABLE 3 The selected flights have been separated into stable (above) and neutral–unstable (below) conditions. Presented are the ID number and corresponding cluster according to Table 2, the flight date, the initial wind speed recovery U_{R0} together with the downstream distance (DD) corresponding to the first horizontal wake traversal behind the wind farm, empirical coefficients (a, b) from the fitting of Gaussian profiles with the exponential function defined by Equation 4, and goodness-of-fit statistics (R^2 values and the root-mean-square error, RME) as measures of the strength of the model for the selected flights shown above in Table 2. The wake length is based on the Gaussian fit to the wind speed recovery U_R defined by Equation 4 and corresponding to the downstream position x where the wind speed within the wake U is 95% of the freestream wind speed U_∞.

ID (cluster)	Date	U_{Ro} [-] (DD [km])	a coefficient	b coefficient	R^2	RMSE	Wake length
		stable atmospheric conditions					[km] (95%)
1 (N-4)	6-Sep-16	0.78 (2.9)	0.24	0.038	0.97	0.01	40
2 (N-4)	7-Sep-16	0.67 (2.1)	0.33	0.038	0.99	0.01	50
3 (N-4)	10-Sep-16	0.73 (4.9)	0.31	0.026	0.97	0.01	65
6 (N-4)	27-May-17	0.66 (1.1)	0.35	0.027	0.87	0.04	70
7 (N-4)	27-May-17	0.78 (1.1)	0.26	0.033	0.91	0.03	50
8 (N-4)	8-Aug-17	0.72 (0.5)	0.27	0.032	0.97	0.02	55
10 (N-3)	15-Aug-17	0.74 (4.5)	0.32	0.054	0.93	0.03	35
11 (N-3)	15-Oct-17	0.75 (1.8)	0.24	0.012	0.96	0.01	>80
Median values			0.29	0.033			53
		neutral–unstable atmospheric conditions					
4 (N-3)	5-Apr-17	0.92 (0.8)	0.14	0.769	0.86	0.01	1.5
5 (N-3)	11-Apr-17	0.79 (0.8)	0.20	0.058	0.86	0.01	24
9 (N-4)	14-Aug-17	0.90 (0.8)	0.09	0.043	0.91	0.01	14
Median values			0.14	0.058			14

The parameterization of the recovery function is adapted to distances where that function dominates the wake evolution, i.e. typically for $x > x_{start}$. However, the wakes inside the wind farm and over the first few kilometers downstream are also determined by the direct wake model and all other parameters of the internal boundary-layer model (deep-array model), which are usually tuned jointly to match the wake conditions *inside* the wind farm, as this is the usual focus of studies using engineering models. Therefore, if the parameters of the wind speed recovery Eq. 6 x_{start} and $x_{50\%}$ are modified to adapt the function to the airborne observations, this also modifies the wake conditions *inside* all considered wind farms (upstream and downstream), as the wake model is the same for the whole modelled region. This means that, strictly speaking, all parameters of the direct wake and internal boundary-layer models would need to be re-tuned to match both the flow conditions inside the wind farms and in the wind speed recovery downstream. As no within-farm data are available here, we do not attempt such a re-tuning, which leads to the overestimation of the modelled wind speeds in the stable case (Figure 8 left). As a consequence, the wind speed conditions in the first 10–20 km downstream (approaching the "upward" bend of the solid black lines in Figure 8) should not be assumed to be modelled correctly and are thus disregarded in the analysis below. This also limits the applicability of this method to downstream distances $x > x_{start}$ where the wind speed recovery is dominant.

In order to estimate the impact of long wakes on the wind farm efficiency (i.e. the ratio of energy yield with and without consideration of wake effects) of distant downstream wind farms, we consider the Butendiek wind farm located about 50 km north of the N-4 cluster, and 25 km southeast of the Dan Tysk wind farm (see Figure 2). We also consider the hypothetical case where all turbines of Butendiek (and of the adjacent wind farm DanTysk) are displaced to the south by 20 km, so that the distance to the N-4 cluster is only 30 km. This distance is somewhat closer to the typical cluster separation in the German EEZ, while it still avoids interference with the direct wake models. Other existing clusters such as N-3, Borkum West/FINO1, or Global Tech I are $>$ 90 km away from the default location of Butendiek, and are thus not considered here as their impact is considered to be largely irrelevant given the recovery functions in Figure 8(left). The calculations are initiated using the wind statistics measured at the FINO1 research platform in the period 2003–2013, corrected to the long-term-averaged wind speed conditions (see Figure 9). For each wind farm, these data are scaled horizontally to the respective wind farm locations using data of a mesoscale simulation with the WRF (Weather research and Forecasting) model. The applied procedure was confirmed by comparison with other meteorological masts, such as the FINO3 platform. In order to obtain comparable energy yields for different scenarios, the all-sector averaged wind speed statistics obtained at each wind farm are either combined with the site-specific wind-sector frequencies (denoted as "allDir" in the following), or assigned only to the sector [165°, 195°] to simulate the flow only from the south (denoted as "onlyS").

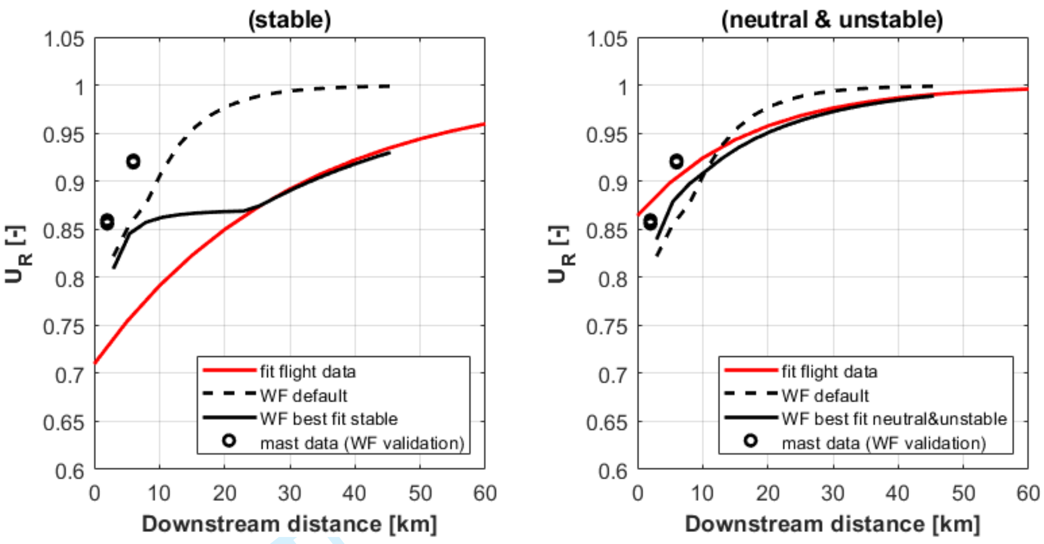

FIGURE 8 Wind speed recovery U_R according to the WindFarmer model as a function of the distance x [km] north of the N-4 cluster. The red line is the recovery function obtained in Figure 7 from the flight observations, the circles correspond to the original measurements used to calibrate the default WindFarmer set-up. The dashed line (identical in both plots) is our modelled wind speed recovery for the N-4 cluster for $U_\infty = 10$ m s^{-1} using the default WindFarmer settings based on the modified PARK (Jensen) model for direct wakes. The solid black lines are the wind speed recovery functions obtained from the best fit to the observations for stable (left) and neutral/unstable (left) conditions above.

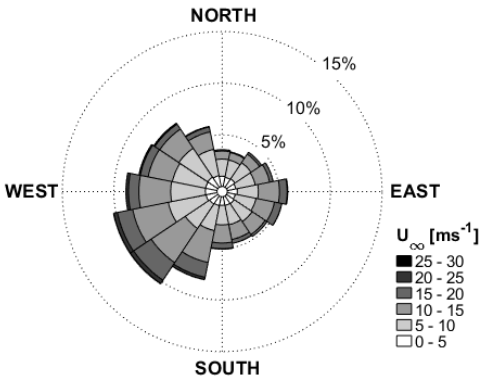

FIGURE 9 Long-term corrected FINO1 wind climate at 91.5 m based on data from 2003–2013.

Since the recovery settings also affect the wakes inside the wind farm, the new settings cannot be compared directly. Instead, we compare the farm efficiency of Butendiek alone and under the impact of the wakes from the N-4 cluster and Dan Tysk (see Table 4). The difference between both impact cases gives an estimate of the effect of the different wind speed recovery settings.

The effect of adding a wind farm (cluster) at 50 km south of Butendiek ("BUT") affects the farm efficiency only marginally under neutral or unstable conditions. In contrast, the effect becomes more significant under stable conditions: for situations for flow directly from the upstream cluster ("onlyS" in our example), the farm efficiency drops by almost 1%. If the annual production were to only occur in stable conditions, but from varying wind directions ("allDir"), the effect would still amount to an efficiency reduction of about 0.4%. If the wind farm (cluster) were only 30 km away ("BUT$_{30km}$"), the effect for stable conditions becomes more pronounced, reaching an "allDir" efficiency reduction of 0.6%.

For a realistic picture, the frequency of stable conditions needs to be known. For the German Bight, Emeis et al.[1] have evaluated the stability conditions using the Monin–Obukhov stability parameter z/L, finding that stable conditions ($z/L \geq 0.04$) occur with an overall frequency of 37% at FINO1. A wind farm surrounded by clusters 30 km away, therefore, experiences an energy-yield loss of $-0.6\% \times 0.37 \approx -0.2\%$. However, there

TABLE 4 Calculated wind farm efficiency for the Butendiek wind farm (BUT) calculated for the wind farm without neighbours ("BUT solo"), and under the impact of the N-4 cluster and the DanTysk wind farm. In the rightmost columns are results from a hypothetical scenario where Butendiek and DanTysk have been moved to the south, so that the distance to the N-4 cluster is reduced to only 30 km ("$\mathrm{BUT}_{30\mathrm{km}}$"). The flow comes either only from the south (i.e. the sector [165°, 195°], "allS"), or from all wind directions using the FINO1 annual wind direction distribution ("allDir"). The results have been derived for neutral/unstable conditions using $x_{\mathrm{start}} = 20\mathrm{D}$ and $x_{50\%} = 100\mathrm{D}$, and for stable conditions using $x_{\mathrm{start}} = 200\mathrm{D}$ and $x_{50\%} = 200\mathrm{D}$.

BUT		**Farm efficiency [%]**					
		BUT			$\mathrm{BUT}_{30\mathrm{km}}$		
		$\mathrm{BUT}_{\mathrm{solo}}$	Cluster	Cluster − $\mathrm{BUT}_{\mathrm{solo}}$	$\mathrm{BUT}_{\mathrm{solo}}$	Cluster	Cluster − $\mathrm{BUT}_{\mathrm{solo}}$
only S	*neutral*	82.6	82.5	−0.2	82.6	82.1	−0.6
	stable	82.0	81.1	−0.9	82.0	79.3	−2.7
allDir	*neutral*	86.8	86.7	−0.1	86.8	86.7	−0.1
	stable	86.7	86.2	−0.4	86.7	86.0	−0.6

is a significant directional dependence: stable conditions occur mainly for the predominant wind directions (south-west), while unstable conditions may prevail for other wind directions. Therefore, the actual effect on a given wind farm needs to be assessed individually depending on the wind direction and stability distribution, and the location of the upstream wind farm clusters. In the specific case of Butendiek, the wake-affected wind directions from the south and north-west are stable for 43% and 30% of the time, respectively, which means that the actual effect of the N-4 cluster and Dan Tysk on Butendiek is reduced to the average one-third, or 0.2% farm-efficiency reduction in the annual average for a wind farm 30 km away. If the wake-generating cluster were, however, located to the south-west, the effect would be at about 60%, and the farm-efficiency reduction would be 0.4%.

Obviously, there is also a clear dependency on distance, and the effect can be expected to increase for wind farms (or clusters) less than 30 km away from each other. This expectation is also confirmed by the flight data presented in Section 5, in particular Figure 7. Unfortunately, due to the above-mentioned limitations in validating the wake-model set-up in the near-downstream range, we could not meaningfully explore this range with the available database. Such an analysis would require a combined investigation of near and far wakes depending on stability. If done properly, such a combined analysis would then enable a stability-dependent readjustment of the models for direct wakes and the internal boundary layer and, thus, facilitate an improved assessment of the absolute production levels.

7 | CONCLUSION

We have analyzed the data from a series of flights collected within the wakes at several downstream distances of two offshore wind farm clusters located in the North Sea during different atmospheric stability conditions. Our findings support the hypothesis[5] that stable stratification leads to significantly longer wakes with a slower wind speed recovery compared with unstable conditions. The results show that the average wake length (defined as when the wind speed has recovered to 95% of the freestream wind speed) under stable conditions exceeds 50 km, while under neutral/unstable conditions, the wake length amounts to 15 km. The default settings of the engineering model WindFarmer have then been modified to account for a slower wind speed recovery in stable stratification, as the observed length of wakes under these conditions greatly exceeds the wake length arising from the default settings.

Examination of the effect of the modified recovery on the farm efficiency of an isolated downstream wind farm reveals that, for distances $>$ 30 km, the calculated reduction of the wind farm efficiency does not exceed 0.5%. This is considered to be a lower limit of the actual economic effect, as distances between most wind farm clusters in the German EEZ and other offshore regions are $<$ 30 km. However, modelling wakes at distances $<$ 30 km downstream requires modification of not only the stability behaviour of the wind speed recovery, but also of the direct wake and internal boundary-layer models. In order to make detailed predictions of the absolute wind farm production, these changes would then also have to be validated against data from inside the wind farms and with respect to stability. As such data have not been available in the WIPAFF project, this is the topic of future research.

Nevertheless, our findings suggest two main conclusions. Firstly, stability plays a major role in the evolution of wakes and can increase the wake length significantly by a factor of three or more. Secondly, the stability climatology should be given more attention when performing energy-yield assessments and wake-model validations, particularly for offshore wind farms. Both the wind speed reduction inside wind farms as well as the wake length in current engineering models appears to be set for neutral conditions, but these are found to underestimate the wake effects for stable conditions.

ACKNOWLEDGMENTS

The authors would like to thank Rolf Hankers, Thomas Feuerle, Helmut Schulz, and Mark Bitter for coordinating and conducting the flight campaigns. The WIPAFF project is funded by the German Federal Ministry of Economic Affairs and Energy under Grant Number FKZ0325783 on the basis of a decision by the German Bundestag.

Conflict of interest

The authors declare no potential conflict of interests.

APPENDIX

APPENDIX A: THEORETICAL ESTIMATION OF THE WIND SPEED RECOVERY IN WIND FARM WAKES

Following Emeis[5,6], the temporal evolution of the wind speed within the wake ($\partial U/\partial t$) may be reduced to considering only its dependence on the vertical momentum exchange while neglecting Coriolis effects by

$$\frac{\partial U}{\partial t} = -\frac{\partial \overline{u'w'}}{\partial z}, \qquad (1)$$

where U is the wind speed within the wake, t is the time, z is the height above the surface, and $\overline{u'w'}$ is the vertical kinematic momentum flux [m^2 s^{-2}]. A bulk parameterization for the momentum flux $\overline{u'w'}$ may be written in terms of an exchange coefficient or eddy viscosity K [m^2 s^{-1}] by

$$\overline{u'w'} = -K\frac{U_\infty - U}{\Delta z}, \qquad (2)$$

where U_∞ is the freestream wind speed, Δz is the vertical separation between the freestream flow and the wake flow, and K is an exchange coefficient, describing the efficiency of momentum between the freestream flow and the wake flow. In this "bulk" formulation, there are only two wind speeds—the wind speed within the wake U and the freestream wind speed U_∞—which enables conversion from differentials ∂z to differences Δz in space. Substituting Equation 2 into the one-dimensional vertical turbulent diffusion Equation 1 gives the first-order differential equation[1] for U as only a function of time t

$$\frac{dU}{dt} + \frac{K}{\Delta z^2}U = \frac{K}{\Delta z^2}U_\infty, \qquad (3)$$

whose solution is

$$U = U_\infty + C\exp\left(-\frac{K}{\Delta z^2}t\right). \qquad (4)$$

Introducing the initial conditions $U(t=0) = U_0 = U_\infty + C$ directly behind the wind farm and solving for the constant C gives the time-dependent wind speed recovery in the wake

$$U_R = \frac{U}{U_\infty} = 1 + \left(\frac{U_0}{U_\infty} - 1\right)\exp\left(-\beta t\right), \qquad (5)$$

where the wind speed recovery rate $\beta = K/\Delta z^2$ [s^{-1}]. Therefore, the wake length is a function of the initial wind speed recovery U_0/U_∞ at $t = 0$, with recovery proceeding exponentially with time at a rate depending on the degree of turbulent exchange K with the freestream flow, and the squared height difference Δz^2 over which the turbulent exchange occurs.

A number of formulations for the initial wind speed recovery U_0/U_∞ have been reported[21]. Assuming that the momentum extracted by the wind farm is replaced by momentum from above via the mechanism of vertical exchange as formulated according to Equation 2, the wind speed recovery immediately downstream of the wind farm U_0/U_∞ is dependent on the stability, the surface roughness, the ambient turbulence intensity, the farm thrust coefficient c_t, and the turbine spacing via see[3,5,6]

$$U_{R0} = \frac{U_0}{U_\infty} = \frac{\frac{h+\Delta z}{\Delta z}I_u + \frac{\Phi_m}{\kappa^2}C_d}{\frac{h+\Delta z}{\Delta z}I_u + \frac{\Phi_m}{\kappa^2}C_{t,eff}}, \qquad (6)$$

---

[1] Of the form $\frac{dy}{dt} + py = r$, where $p = \frac{K}{\Delta z^2}$ and $r = \frac{K}{\Delta z^2}U_\infty$ are constant in t.

where h is the turbine height, I_u is the ambient turbulence intensity, ϕ_m is the stability-dependent dimensionless wind shear (see Appendix B), and κ is the von Karman constant. The effective drag coefficient $C_{t,eff}$ is the sum of surface roughness C_d and the wind farm thrust coefficient c_t,

$$C_{t,eff} = c_t + C_d, \tag{7}$$

with [22,21]

$$c_t = \frac{\pi}{8}\frac{C_T}{(s/D)^2}, \tag{8}$$

where C_T is the wind speed dependent turbine thrust coefficient, s [m] is the mean turbine separation, and D is the turbine diameter.

Therefore, in addition to the parameters determining the wind farm layout and operation (C_T, s/D, h), the stability enters into the formulation for the initial wind speed recovery through the stability-dependent dimensionless wind shear Φ_m (see Appendix B for a further description of this dependence), and also determines the wind speed recovery through the exchange coefficient by (also see Appendix B)

$$K = \frac{\kappa u_* h}{\Phi_m}, \tag{9}$$

where $u_* = \left(\overline{u'w'}_0^2\right)^{1/4}$ is the friction velocity, with $\overline{u'w'}_0$ the kinematic momentum flux at the surface. Finally, letting Δz equal the rotor diameter D, assuming this to be the length scale in Equation 2 over which vertical exchange occurs, then the wind speed recovery rate in Equation 5 becomes

$$\beta = \frac{\kappa u_* h}{\Phi_m D^2}. \tag{10}$$

APPENDIX B: STABILITY FORMULATIONS

Monin–Obukhov similarity theory reduces the dimensionless wind shear Φ_m at the height z over the surface to a single function f of the Monin–Obukhov stability parameter $\zeta = z/L$ [37],

$$\Phi_m = \frac{\kappa z}{u_*}\frac{\partial U}{\partial z} = f(\zeta), \tag{11}$$

where κ is the von Karman constant, and f represents the Monin–Obukhov similarity functions dependent only on the Monin–Obukhov similarity parameter ζ. The logarithmic wind speed profile

$$U = \frac{u_*}{\kappa}\left[\ln\left(\frac{z}{z_0}\right) - \Psi(\zeta)\right], \tag{12}$$

is obtained by integration of Equation 11, where z_0 is the roughness length, and the function

$$\Psi = \int_0^{\zeta} \frac{1-\Phi_m(\zeta)}{\zeta}\zeta, \tag{13}$$

where

$$\Phi_m(\zeta \geq 0) = 1 + 5\zeta \tag{14}$$

and

$$\Psi_m(\zeta \geq 0) = -5\zeta \tag{15}$$

in stable conditions ($\zeta > 0$) and

$$\Phi_m(\zeta < 0) = (1 - 16\zeta)^{-1/4} \tag{16}$$

and

$$\Psi_m(\zeta < 0) = 2\ln\left(\frac{1+X}{2}\right) + \ln\left(\frac{1+X^2}{2}\right) - 2\arctan X + \frac{\pi}{2} \tag{17}$$

in unstable conditions ($\zeta < 0$), with $X = (1-16\zeta)^{1/4}$. The Monin–Obukhov stability parameter at hub height $z = h$ is

$$\frac{h}{L} = -\frac{\kappa h\,(g/T)\,H}{u_*^3}, \tag{18}$$

where g/T is the buoyancy parameter, with g the acceleration due to gravity, and T the air temperature. The friction velocity $u_*^2 \equiv -\overline{w'v'}$ and heat flux H can be written in terms of the surface drag coefficient C_d and surface heat exchange C_H coefficients by

$$u_*^2 = C_d\overline{U}^2, \tag{19}$$

and

$$H = -C_H\overline{U}\left(\overline{\theta} - T_0\right), \tag{20}$$

respectively, to yield the bulk Richardson number R_{bh} at hub height multiplied by a factor of 10

$$\frac{h}{L} \approx 10R_{bh} = \frac{10\,(g/T)\,h\left(\overline{\theta} - T_0\right)}{\overline{U}^2}, \tag{21}$$

assuming the exchange coefficients are approximately equal $C_d \approx C_H \sim 1 \times 10^{-3}$, and the ratio $\kappa/\sqrt{C_d} \approx 10$.

$$Ri_{bh} = \frac{h\,(g/T)\,\Delta\overline{\theta}_v}{\overline{U^2}}, \tag{22}$$

where h is the flight altitude, and $\Delta\overline{\theta}_v = \theta_v - T_{v0}$ is the virtual potential temperature difference between the sea surface and the flight altitude averaged over the horizontal traversals. For the calculation of the temperature difference $\Delta\overline{\theta}_v$, the sea-surface temperature (T_0, SST) is estimated by extrapolating measured profiles of the temperature T(z) down to the surface, with the relative humidity at the sea surface assumed as 100% and converted to the specific humidity Q_0, yielding the virtual potential temperature at the surface as $T_{v0} = T_0\,(1 + 0.61Q_0)$. The potential temperature θ at flight altitude is calculated from $\theta_z = T_z + (g/C_p)\,z$, where T_z is the measured temperature, g/C_p is the adiabatic lapse rate, with C_p the specific heat of dry air. The virtual potential temperature at height z may then be inferred from the specific heat Q_z at height z from $\theta_v = \theta_z\,(1 + 0.61Q_z)$.

References

1. Emeis S, Siedersleben S, Lampert A, et al. Exploring the wakes of large offshore wind farms. *Journal of Physics: Conference Series* 2016; 753: 092014. doi: 10.1088/1742-6596/753/9/092014
2. Nygaard N, Newcombe A. Wake behind an offshore wind farm observed with dual-Doppler radars. *Journal of Physics: Conference Series* 2018; 1037: 072008. doi: 10.1088/1742-6596/1037/7/072008
3. Frandsen S. On the wind speed reduction in the center of large clusters of wind turbines. *Journal of Wind Engineering and Industrial Aerodynamics* 1992; 39(1): 251-265. doi: https://doi.org/10.1016/0167-6105(92)90551-K
4. Frandsen S, Barthelmie R, Pryor S, et al. Analytical modelling of wind speed deficit in large offshore wind farms. *Wind Energy* 2006; 9(1-2): 39-53. doi: 10.1002/we.367
5. Emeis S. A simple analytical wind park model considering atmospheric stability. *Wind Energy* 2010; 13(5): 459-469. doi: 10.1002/we.367
6. Emeis S. *Wind Energy Meteorology - Atmospheric Physics for Wind Power Generation.* Springer. 2 ed. 2018.
7. Patrick V, Hahmann AN, Badger J. *Wake Effects of Large Offshore Wind Farms - a study of the Mesoscale Atmosphere*. PhD thesis. DTU Wind Energy, Denmark; 2014.
8. Christiansen M, Hasager C. Wake effects of large offshore wind farms identified from satellite SAR. *Remote Sensing of Environment* 2005; 98(2): 251-268. doi: https://doi.org/10.1016/j.rse.2005.07.009
9. Djath B, Schulz-Stellenfleth J, Cañadillas B. Impact of atmospheric stability on X-band and C-band synthetic aperture radar imagery of offshore windpark wakes. *Journal of Renewable and Sustainable Energy* 2018; 10(4). doi: 10.1063/1.5020437
10. Ahsbahs T, Badger M, Volker P, Hansen KS, Hasager C. Applications of satellite winds for the offshore wind farm site Anholt. *Wind Energy Science* 2018; 3: 573-588. doi: 10.5194/wes-3-573-2018
11. Platis A, Siedersleben S, Bange J, et al. First in situ evidence of wakes in the far field behind offshore wind farms. *Scientific reports* 2018; 8(1). doi: 10.1038/s41598-018-20389-y
12. Foreman R, Emeis S, Cañadillas B. Half-Order Stable Boundary-Layer Parametrization Without the Eddy Viscosity Approach for Use in Numerical Weather Prediction. *Boundary-Layer Meteorology* 2015; 154(2): 207–228. doi: 10.1007/s10546-014-9969-4
13. Dörenkämper M, Optis M, Monahan A, Steinfeld G. On the Offshore Advection of Boundary-Layer Structures and the Influence on Offshore Wind Conditions. *Boundary-Layer Meteorology* 2015; 155: 459-482. doi: 10.1007/s10546-015-0008-x
14. Jensen N. *A note on wind generator interaction.* Risø National Laboratory . 1983.
15. Katic I, Højstrup J, Jensen N. A Simple Model for Cluster Efficiency. In: Palz W, Sesto E., eds. *EWEC'86. Proceedings. Vol. 1*A. Raguzzi; 1987: 407–410.
16. Ainslie J. Calculating the flow field in the wake of wind turbines. *Journal of Wind Engineering and Industrial Aerodynamics* 1988; 27(1): 213 - 224. doi: https://doi.org/10.1016/0167-6105(88)90037-2

17. Brower M, Robinson N. The OpenWind deep-array wake model: development and validation. tech. rep., AWS Truepower; Albany, NY, USA: 2009.

18. DNV-GL . WindFarmer v.5.2 Theory Manual. tech. rep., Garrad Hassan and Partners, Ltd.; 2013a.

19. Beaucage P, Robinson N, Brower M, Alonge C. Overview of six commercial and research wake models for large offshore wind farms. In: ; 2012. Proceedings EWEA 2012, Copenhagen.

20. Stevens RJAM, Gayme DF, Meneveau C. Generalized coupled wake boundary layer model: applications and comparisons with field and LES data for two wind farms. *Wind Energy* 2016; 19(11): 2023-2040. doi: 10.1002/we.1966

21. Peña A, Rathmann O. Atmospheric stability-dependent infinite wind-farm models and the wake-decay coefficient. *Wind Energy* 2014; 17(8): 1269-1285. doi: https://doi.org/10.1002/we.1632

22. Frandsen S, Barthelmie R, Rathmann O, et al. *Summary Report: The Shadow effect of large wind farms: measurements, data analysis and modelling: Risø-R-1615 (EN).* Risø National Laboratory. 1 ed. 2007.

23. Westerhellweg A, Cañadillas B, Kinder F, Neumann T. Wake Measurements at alpha ventus – Dependency on Stability and Turbulence Intensity. *Journal of Physics: Conference Series* 2014; 555: 012106. doi: 10.1088/1742-6596/555/1/012106

24. Javaheri A, Cañadillas B. Wake Modeling of an Offshore Wind Farm Using OpenFOAM. *DEWI Magazine* 2013; 43(04).

25. Barthelmie RJ, Frandsen ST, Rathmann O, et al. *Flow and wakes in large wind farms: Final report for UpWind WP8.* Risø DTU National Laboratory for Sustainable Energy . 2011.

26. Schneemann J, Hieronimus J, S. JSL, Kühn M. Offshore wind farm flow measured by complementary remote sensing techniques: radar satellite TerraSAR-X and lidar windscanners. *Journal of Physics: Conference Series* 2015; 625. doi: 10.1088/1742-6596/625/1/012015

27. Hasager C, Astrup P, Christiansen M, Nielsen M, Barthelmie R. Wind resources and wind farm wake effects offshore observed from satellite. In: European Wind Energy Association (EWEA); 2006.

28. Hasager C, Vincent P, Badger J, et al. Using Satellite SAR to Characterize the Wind Flow around Offshore Wind Farms. *Energies* 2015; 8(6): 5413–5439. doi: 10.3390/en8065413

29. Siedersleben SK, Platis A, Lundquist JK, et al. Evaluation of a Wind Farm Parametrization for Mesoscale Atmospheric Flow Models with Aircraft Measurements. *Meteorologische Zeitschrift* 2018; 27(5): 401-415. doi: 10.1127/metz/2018/0900

30. Siedersleben SK, Lundquist JK, Platis A, et al. Micrometeorological impacts of offshore wind farms as seen in observations and simulations. *Environmental Research Letters* 2018; 13(12). doi: 10.1088/1748-9326/aaea0b

31. Foreman R, Emeis S. Revisiting the Definition of the Drag Coefficient in the Marine Atmospheric Boundary Layer. *Journal of Physical Oceanography* 2010; 40(10): 2325-2332. doi: 10.1175/2010JPO4420.1

32. Corsmeier U, Hankers R, Wieser A. Airborne turbulence measurements in the lower troposphere onboard the research aircraft Dornier 128-6, D-IBUF. *Meteorologische Zeitschrift* 2001; 10(4): 315-329. doi: 10.1127/0941-2948/2001/0010-0315

33. Bundesnetzagentur . EEG-Anlagenstammdaten. 2017. https://www.bundesnetzagentur.de/DE/Sachgebiete/ElektrizitaetundGas/Unternehmen_Institutionen/ErneuerbareEnergien/ZahlenDatenInformationen/EEG_Registerdaten/EEG_RegDaten_FoerdSaetze.html Accessed April 1, 2018.

34. Entwurf Flächenentwicklungsplan 2019 für die deutsche Nord- und Ostsee. tech. rep., Bundesamt für Seeschiffahrt und Hydrographie; 2018. https://www.bsh.de/DE/THEMEN/Offshore/Meeresfachplanung/_Anlagen/Downloads/Aktuelles_FEP_Entwurf_FEP2.pdf?__blob=publicationFile&v=3.AccessedApril15,2019.

35. Göçmen T, van der Laan P, Réthoré PE, Peña Diaz A, Chr. Larsen G, Ott S. Wind turbine wake models developed at the technical university of Denmark: A review. *Renewable and Sustainable Energy Reviews* 2016; 60: 752-769. doi: 10.1016/j.rser.2016.01.113

36. DNV-GL . WindFarmer v.5.2 Validation Report. tech. rep., Garrad Hassan and Partners, Ltd.; 2013b.

37. Stull R. *An Introduction to Boundary Layer Meteorology.* Kluwer Academic Publishers . 1988.